Wide-swath altimetric satellite data assimilation with structured-error detrending

Sammy Metref[1,*], Emmanuel Cosme[1], Florian Le Guillou[1,] Julien Le Sommer[1], Jean-Michel Brankart[1] and Jacques Verron[1,2]

[1] *Université Grenoble Alpes, CNRS, IRD, IGE, Grenoble, France.*
[2] *Ocean Next, Grenoble, France.*

[*] Correspondence: sammy.metref@univ-grenoble-alpes.fr

Wide-swath altimetric satellite data assimilation with structured-error detrending

Sammy Metref [1,*], Emmanuel Cosme [1], Florian Le Guillou [1], Julien Le Sommer [1], Jean-Michel Brankart [1] and Jacques Verron [1,2]

[1] *Université Grenoble Alpes, CNRS, IRD, IGE, Grenoble, France.*
[2] *Ocean Next, Grenoble, France.*

Correspondence*:
Sammy Metref, MEOM/IGE, UGA, CS 40 700, 38058, Grenoble, Cedex 9, FRANCE.
sammy.metref@univ-grenoble-alpes.fr

ABSTRACT

For decades now, satellite altimetric observations have been successfully integrated in numerical oceanographic models using data assimilation (DA). So far, sea surface height (SSH) data were provided by one-dimensional nadir altimeters. The next generation Surface Water and Ocean Topography (SWOT) satellite altimeter will provide two-dimensional wide-swath altimetric information with an unprecedented high resolution. This new type of SSH data is expected to strongly improve altimetric assimilation. However, the SWOT data is also expected to be affected by spatially structured errors and, hence, can not be assimilated as easily as nadir altimeters. The present paper proposes to embed a state-of-the-art error detrending method for the SWOT data into an ensemble-based DA scheme. This new detrended-DA scheme is implemented and tested in a simple SSH reconstruction problem using artificial SWOT data and a quasi-geostrophic model. The results show that, in an energetic large scale region and when the region is intensely observed, the detrended-DA – in comparison to the classical DA – reduces the root-mean-square-error (RMSE) of the reconstruction in SSH, relative vorticity and surface currents and slightly improves the relative error spectrum and spectral coherence of the SSH signal at mesoscale (100-200km). In a less energetic region, the detrended-DA reduces on average by more than 50% the RMSE in SSH therefore allowing a significantly more accurate reconstruction of SSH at mesoscale in terms of relative error spectrum, spectral coherence and power spectral density.

Keywords: sea surface height, reconstruction, SWOT, OSSE, ensemble Kalman filter, NATL60, quasi-geostrophic model

1 INTRODUCTION

In operational oceanography, the assimilation of altimetric data has become crucial to control the time evolution of oceanic surface flows as well as its impact to the circulation in the deeper ocean (Fu and Cazenave, 2000; Chelton et al., 2001; Fu and Chelton, 2001; Morrow and Le Traon, 2012; Stammer and Cazenave, 2018). Indeed, the increasing number of satellite missions providing a large quantity of along track altimetric measurements has allowed oceanographic operational centers to better understand and to better constrain the sea surface height (SSH) and the associated surface currents in their models.

Assimilating along track altimetric data has led to more accurate representations and predictions of the oceanic properties at large and meso-scales, i.e., down to 150 km at midlatitudes.

The new Surface Water and Ocean Topography (SWOT) satellite altimeter, planned for launch in 2021, will bring a large amount of two-dimensional high resolution data that should significantly improve altimetric assimilation. The SWOT satellite will use a Ka-band radar interferometer instrument mapping the globe with a repeat period of 21 days and generating a 120 km swath (with a 20km gap at its center) of SSH data. The final data products are expected to reach a 15-30km effective resolution (Morrow et al., 2019). The high resolution two-dimensional SWOT data will, however, inevitably lead to new challenges for SSH data assimilation. For instance, the SWOT data are expected to be impacted by large spatially structured errors, especially in the across track direction (Esteban-Fernandez, 2017; Gaultier et al., 2016; Metref et al., 2019).

The two-dimensional spatially structured SWOT errors can not be taken into account with a non diagonal observation error covariance matrix in the assimilation scheme as the computational cost would be prohibitive (see for instance Oke et al., 2008 for oceanography or Liu and Rabier, 2002 for meteorology). Several techniques have been proposed to assimilate observations with correlated errors while compensating for the diagonal observation error covariance matrix hypothesis (Stewart et al., 2008, 2013; Miyoshi et al., 2013; Waller et al., 2014; Brankart et al., 2009; Ruggiero et al., 2016). In the present paper, we make the case that the SWOT errors will be so large and so non-locally correlated that SWOT data should not be assimilated as is. Instead, we propose to assimilate a modified SWOT data.

We embed the detrending procedure that was developed in the error reduction method proposed by Metref et al. (2019) into an assimilation scheme, the ensemble tranform Kalman filter (Bishop et al., 2001). The detrending consists, first, in projecting the data onto the across-track trends that correspond to the SWOT errors spatial structure. The detrended SWOT data that are then assimilated, are the residual of this projection. The detrended SWOT data are not a direct observation of SSH but a proxy of SSH. Hence, to keep the assimilation process consistent, the detrending must be embedded in the observation operator of the DA scheme.

The goal of this paper is to evaluate the improvement brought by this new detrended-DA scheme on a fully-noised SWOT data assimilation cycled in time. The detrended-DA scheme is tested for solving an SSH map reconstruction problem, in order to assess in a simplified three-dimensional problem (sea surface and time) the performance of the scheme. The numerical experiments are observation system simulation experiments (OSSE), set in two regions of different energetic intensities: the Gulf Stream region, hereafter called GULFSTREAM (with energetic flows at both large and meso-scales) and the Porcupine Abyssal plain region, hereafter called OSMOSIS (with energetic flows at mesoscale but relatively weak large scale flow). These two regions exhibit very distinct characteristics in terms of SSH variability and observation frequency. Using the SWOT simulator (SWOT simulator, 2016; Gaultier et al., 2016), artificial SWOT data with their corresponding noise are created from outputs of a North Atlantic high resolution numerical simulation (NATL60, 2018) generated with the NEMO 3.5 (Nucleus for European Modelling of the Ocean) modelling system (Madec, 2015). These artificial SWOT data are then assimilated in a one and half layer quasi-geostrophic (QG) model. We compare the performances of an ensemble Kalman filter (EnKF) when assimilating the noise free data (*EnKF no noise*), the data only noised by the uncorrelated instrumental error (*EnKF karin noise*, see Section 2.1), the fully noised data (*EnKF full noise*) and the fully noised data that have been detrended (*EnKF detrended full noise*). The performances of the reconstructions are evaluated over a two-month period in comparison to the supposed truth (i.e., the NATL60 simulation) with root-mean-square errors (RMSE) on the SSH, the relative vorticity ζ and the surface currents (u, v) ; and with power spectral densities, relative error spectra and spectral coherences on the SSH.

The paper is structured as follows. Section 2 recalls the errors expected to impact the SWOT data, describes the detrending procedure from Metref et al. (2019) and provides the theoretical grounds to embed the detrending in an ensemble-based DA scheme. Section 3 implements this new detrended-DA scheme and tests it in the assimilation problem of SSH reconstruction using a one and a half layer QG model. Conclusions and perspectives are drawn in Section 4.

2 DETRENDED-DATA ASSIMILATION METHOD

2.1 SWOT errors

The SWOT project team maintains a document describing the expected SWOT error budget (Esteban-Fernandez, 2017). Based on that error budget, a simulator of SWOT-like observations was developed by the NASA Jet Propulsion Laboratory (Gaultier et al., 2016). This SWOT simulator allows the scientific community to produce artificial SWOT data for them to be used in OSSE. The SWOT simulator interpolates any SSH simulation onto the SWOT swath groundtrack and computes and adds a realization of the SWOT errors. The SWOT simulator only generates the main SWOT errors described in Esteban-Fernandez (2017): Ka-Band Radar Interferometer (KaRIn) error, residual roll error, phase error, baseline dilation error, timing error, wet-troposphere error. Of those six errors, only four are concerned by the detrending procedure. The KaRIn error is the instrumental random error, uncorrelated in space with a non-constant variance across track (see the Appendix). This uncorrelated error is not taken into account in the detrending procedure since uncorrelated errors are by construction well dealt with by the assimilation process, as confirmed by the results in Section 3. The wet-troposphere error corresponds to the signal path delay due to the variability of the water vapor content in the troposphere. This delay introduces isotropically correlated errors. In the detrending formulation, we neglect the wet-troposphere error as it has a two-dimensional spatial structure. Moreover, the wet-troposphere error is not expected to be the largest contributing error. However, introducing a two-dimensional detrending or combining the across-track detrending with DA methods for locally correlated errors (Brankart et al., 2009; Ruggiero et al., 2016; Yaremchuk et al., 2018) in order to take into account the wet-troposphere error should be investigated in future studies and should further improve the results. The four errors concerned by the detrending procedure are the timing error, the roll error, the baseline dilation error and the phase error. The timing error is only due, at first order, to a timing drift in the instrument signal propagation and can be assumed to be constant across track. The roll error is generated by the satellite roll angle, which impacts the measurement linearly across-track and is zero at its center. The baseline dilation error comes from the length variation of the satellite mast which creates a deviation between the two calibrated sensor signals. This creates a quadratic error distribution in the across-track direction. Finally, the phase error is due to the relative phase variations of the two sensors which produce cross-track linear errors independent in each half-swath. The across-track structure of the four cumulated sources of error can be modelized by:

$$e_{\text{total}} = \alpha_0 + \alpha_1 x_c + \alpha_2 x_c^2 + [\alpha_3 + \alpha_4 x_c]\mathcal{H}(-x_c) + [\alpha_5 + \alpha_6 x_c]\mathcal{H}(x_c), \tag{1}$$

with x_c the across-track grid points ; $\mathcal{H}(x)$ the Heaviside function which equals 1 when $x > 0$ and 0 otherwise ; and where $\{\alpha_i\}_{i=0,\ldots,6}$ are unknown constant coefficients. In Equation (1), the first term corresponds to the timing error, the second to the roll error, the third to the baseline dilation error and the last two terms correspond to the phase error in each half-swath. Similarly to Metref et al. (2019), we justify the assumption that the coefficients $\{\alpha_i\}_{i=0,...,6}$ are constant along-track by the relatively small size of the regions of interest.

2.2 Detrending procedure

In order to detrend the part of the SWOT signal h impacted by the errors, we first calculate the projection of h onto the subspace spanned by the modelized errors in Equation (1). This projection is performed by calculating the coefficients minimizing the following cost function:

$$\mathcal{J}(\{\alpha_i\}_{i=0,...,6}) = \sum_{x_c=-\frac{n_c}{2}}^{\frac{n_c}{2}} \Big(\bar{h}(x_c) - \{\alpha_0 + \alpha_1 x_c + \alpha_2 x_c^2 + [\alpha_3 + \alpha_4 x_c]\mathcal{H}(-x_c) + [\alpha_5 + \alpha_6 x_c]\mathcal{H}(x_c)\}\Big)^2, \quad (2)$$

with n_c the number of across track grid points and where $\bar{h}$ is the SWOT signal h averaged along-track on the region.

The detrending is then defined as the residual between the SWOT signal h and the projection of $\bar{h}$:

$$\mathcal{T}(h(x_c, x_a)) = h(x_c, x_a) - \{\alpha_1 x_c + \alpha_2 x_c^2 + [\alpha_3 + \alpha_4 x_c]\mathcal{H}(-x_c) + [\alpha_5 + \alpha_6 x_c]\mathcal{H}(x_c)\}, \quad (3)$$

for all across- and along-track grid points (x_c, x_a) and with $\{\alpha_i\}_{i=1,...,6}$ the coefficients minimizing $\mathcal{J}$ in Equation (2). Note that the constant term of the projection α_0 has to be removed from Equation (3) due to the fast variations of the timing error that are not in agreement with the constant projection in the along-track direction (more details in Metref et al., 2019).

2.3 Embedding the detrending procedure in data assimilation

In the present paper, we make the case that the SWOT data h are too strongly affected by large and correlated noises to be directly assimilated. Indeed, the presence of correlated errors leads to non-diagonal observation error covariance matrices which most DA schemes need to invert. In large dimension, the cost of this inversion quickly becomes prohibitive for non-diagonal observation error covariance matrices and, in practice, it is common to make the assumption that the matrices are diagonal hence ignoring the error correlations. This assumption can no longer stand for the strongly spatially correlated SWOT errors. However, by construction and as shown in Metref et al. (2019), the detrending $\mathcal{T}$ reduces those correlations. Hence, in this paper, we propose to assimilate $h^{\mathrm{o}} = \mathcal{T}(h)$ instead of h. In order to be consistent, it is important to realize that $\mathcal{T}(h)$ is not a direct observation of SSH but a proxy. Therefore, the observation operator linking the model state to the observation must also include the detrending. If we note h^{m} the SSH described by the model and $\mathcal{I}$ the interpolation from the model grid to the SWOT grid, the observation operator is now:

$$H \equiv \mathcal{T} \circ \mathcal{I} \quad (4)$$

and the innovation, i.e. the difference between the model state and the observation in the observation space, becomes $[h^{\mathrm{o}} - \mathcal{T}(\mathcal{I}(h^{\mathrm{m}}))]$.

The detrending procedure can be embedded in any DA method that uses the observation operator. The algorithms for the detrending of the SWOT data and for the embedding of the detrending in the observation operator are illustrated in Figure 1.

In this study, we focus on ensemble-based DA. In particular, the numerical experiments presented in Section 3 implement the detrending procedure in an ensemble Kalman filter (EnKF). In practice, this implementation corresponds to $N_e + 1$ detrendings at each analysis time step, where N_e is the number of ensemble members: N_e detrendings for the ensemble and one detrending for the SWOT data. Note that the computational cost for these $N_e + 1$ operations remains small in comparison with the DA process itself.

3 NUMERICAL EXPERIMENTS

3.1 Experimental setup

In the following OSSE, we consider the North Atlantic high resolution (1/60° at the Equator) numerical simulation (NATL60, 2018), generated with the NEMO model, as the true ocean. The NATL60 simulation has been used in several studies (Fresnay et al., 2018; Amores et al., 2018; Metref et al., 2019) and is one of the most advanced basin-scale high resolution simulation available to this day (approximately 10km effective resolution).

An important feature of this study is the evaluation of the detrending-DA scheme in a DA problem cycled in time. The assimilation experiments start on October 1st, 2012 and end on December 31st, 2012. Only the last two months of the experiments are considered for the evaluation in order to let the DA processes converge, i.e., the diagnostics are performed from November 1st, 2012 to December 31st, 2012 (respectively referred to as $t = 0$ and $t = 61$ in Figure 5 and 6). During these two months, the SWOT satellite almost completes three repeat cycles of the globe.

Figure 2 shows a snapshot of the SSH (in meters), in the two regions of interest: GULFSTREAM (left panel) and OSMOSIS (right panel), on November 4, 2012. The GULFSTREAM region spreads from 33°N to 43°N in latitude and 53°W to 65°W in longitude. The OSMOSIS region (spread from 45°N to 55°N in latitude and 11°W to 19°W in longitude) is part of the Porcupine Abyssal plain region and was intensively studied during the OSMOSIS campaign (Buckingham et al., 2016). The two regions differ in the intensity of their SSH variations. GULFSTREAM is zonally crossed by the Gulf Stream current which has a strong signature on SSH with heights reaching one meter. Whereas, the OSMOSIS region rarely reaches 20 cm SSH but displays various small eddies. Also, the difference in latitude between the regions impacts the frequency of observation by the SWOT satellite. The OSMOSIS region is at least partially observed every day when the GULFSTREAM region can be unobserved during 5 days straight. The two regions hence provide two distinct situations that SWOT will encounter.

From the true ocean, artificial SWOT data are created using the SWOT simulator (see Appendix A of Metref et al., 2019, for the detailed SWOT simulator parameters). The SWOT data were generated on the “Science orbit” with a repeat cycle of approximately 21 days. In the experiments, four DA processes will be compared: (i) *EnKF no noise*, which assimilates the SWOT data without noise ; (ii) *EnKF karin noise*, which assimilates the SWOT data with only the uncorrelated KaRIn noise ; (iii) *EnKF full noise*, which assimilates the SWOT data with all noises available on the simulator (see Section 2.1) and (iv) *EnKF detrended full noise*, which assimilates the detrended fully noised SWOT data.

The model used for SSH propagation is a one and a half layer QG model as described in Ubelmann et al. (2015). The QG model propagates the SSH by advecting the corresponding potential vorticity with the geostrophic currents. The first Rossby radius of deformation used are approximately 36 km and 22 km in the GULFSTREAM and OSMOSIS region, respectively. The model time step is 10 minutes.

The DA scheme implemented is an ensemble transform Kalman filter (Bishop et al., 2001) with domain localization (Hunt et al., 2007) and set with a 30 km localization radius and a 90 km localization cutoff. The filter is used sequentially with a 3h cycle time step, i.e., an analysis is performed every three hours if an observation is available in the region at that time. The filter runs with 50 ensemble members, which are initialized by randomly selecting NATL60 SSH fields between April and September 2013. An inflation of 1% is applied on the ensemble before every analysis for all assimilations. The observation error covariance matrix $\mathbf{R}$ is assumed diagonal for the four assimilations, as previously discussed. For the *EnKF no noise* assimilation, $\mathbf{R}$ is prescribed constant along the diagonal of standard deviation 2 cm. For the *EnKF karin noise* assimilation, $\mathbf{R}$ is prescribed with the error standard deviations used to create the KaRIn error (see the Appendix). The *EnKF full noise* and *EnKF detrended full noise* assimilations use the same matrix $\mathbf{R}$ as the *EnKF karin noise* assimilation but with an inflation of 30% and 10% respectively in GULFSTREAM and of 40% and 20% respectively in OSMOSIS. These inflation coefficients were manually tuned to provide the smallest SSH RMSE (not shown here).

3.2 Results

Figure 3 and 4 display, in GULFSTREAM and OSMOSIS respectively, the SSH reconstructions (left columns) obtained with the four assimilations corresponding to the true SSH fields in Figure 2. The right columns of Figure 3 and Figure 4 are the point-wise differences with the true SSH fields. These fields correspond to November 4, 2012, more than a month after the beginning of the assimilation processes. In GULFSTREAM, a SWOT pass has just been assimilated which explains the white track on the right of the panels corresponding to the local analysis of the EnKF. In OSMOSIS, no analysis was recently performed at day November 4, 2012 but the error trends of previous observations that were forecasted remain visible in the *EnKF full noise* reconstruction. This confirms the importance of assessing the impact of the SWOT noise and the detrended-DA scheme in an assimilation problem cycled in time.

The first result is that the reconstruction produced by the assimilation without noise and with the KaRIn noise only are very similar. This indicates that, as expected, the EnKF seems well suited to deal with the uncorrelated KaRIn noise. However, in both GULFSTREAM and OSMOSIS cases, the EnKF assimilating the full noise is very much affected by the spatially structured noise. As previously mentioned, in both cases, the satellite tracks and the error trends impact the reconstructions. This is particularly visible on the recently assimilated SWOT track on the right of the panels in GULFSTREAM, where a large error trend appears in the *EnKF full noise* reconstruction. The detrended-DA does not entirely remove the spatially structured errors impact but strongly reduces it. Unlike the SSH fields reconstructed by *EnKF full noise*, the fields reconstructed by *EnKF detrended full noise* seem, visually at least, geophysical.

In order to quantify the improvement brought by the detrended-DA scheme, we compute the RMSE of the SSH reconstructed fields at each time to obtain RMSE time series. The RMSE of a 2D reconstructed field $\mathbf{x} = \{x\}_{i=1,\dots N}$ with respect to the true field $\mathbf{x}^{\mathrm{t}} = \{x^{\mathrm{t}}\}_{i=1,\dots N}$ is calculated as such:

$$\mathrm{RMSE}(\mathbf{x}) = \sqrt{\frac{1}{N}\sum_{i=1}^{N}(x_i - x_i^{\mathrm{t}})^2} \tag{5}$$

with N the number of grid points. Figure 5 shows the RMSE time series calculated in GULFSTREAM during the two-month experiment for the SSH, the relative vorticities ζ and the currents (u, v). The RMSE show the cycles of the SWOT track crossing the GULFSTREAM region with approximately 9-day periods when the region is well observed and 5-day periods with almost no observation in the region. The first important result of these experiments is the very close RMSE on all four variables produced by the assimilation of the noise free SWOT data and the KaRIn noise only SWOT data. This means that in terms of RMSE the KaRIn error is being well delt with by the EnKF assimilation scheme. During the time periods without observation, *EnKF full noise* and *EnKF detrended full noise* assimilations have approximately the same errors. But when the region is well observed, the detrended-DA scheme helps reduce the RMSE. At day 39, for instance, the SSH RMSE of the *EnKF detrended full noise* is half the one of the *EnKF full noise*. The RMSE on average over the two-month experiment are listed in Table 1. The averaged RMSE confirm the improvement brought by the detrended-DA scheme. Indeed, in GULFSTREAM, the averaged SSH RMSE of the reconstruction is 9.3 cm without noise, 12.1 cm with full noise, but is reduced to 10.9 cm by the detrending. Because of the smaller magnitude of the SSH variations in OSMOSIS, the impact of the SWOT errors on the reconstruction in that region is very substantial. Figure 6 shows the large benefit of using the detrended-DA in the OSMOSIS region with, at day 15 for example, a SSH RMSE reduction of over 60%. On average (see Table 1), the SSH RMSE ratio: RMSE[*EnKF full noise*] / RMSE[*EnKF no noise*] is approximately 337% and is reduced by the detrended-DA to a ratio of approximately 153%.

The SWOT errors were designed to respect error specifications in the spectral domain, however, the RMSE does not allow to assess the reconstructions independently in the different spatial scales. Moreover, the SWOT mission objectives were defined in terms of spectra, with a resolution of 15-30km (Morrow et al., 2019). Hence, it is necessary to assess the impact of the full SWOT noise on the small scales. Here, we perform three two-dimensional spectral diagnostics on the SSH: the power spectral density, the relative error spectrum and the spectral coherence. The power spectral density (PSD) is a 2D wavenumber spectrum which describes the energy of the signal at the different spatial scales. The relative error spectrum $\mathcal{R}$ compares an estimated signal $\mathbf{x}$ to a true signal $\mathbf{x}^{\mathrm{t}}$ such that:

$$\mathcal{R}(\mathbf{x}) = 1 - \frac{PSD(\mathbf{x} - \mathbf{x}^{\mathrm{t}})}{PSD(\mathbf{x}^{\mathrm{t}})} \quad . \tag{6}$$

When the energy of the residue $\mathbf{x} - \mathbf{x}^{\mathrm{t}}$ is small compared with the energy of the true signal $\mathbf{x}^{\mathrm{t}}$, $\mathcal{R}$ should be close to 1. And finally, the spectral coherence is a normalized cross spectrum and describes the spatial correlations between two signals (here, the estimated signal and the true signal) at the different scales. The spectral coherence should be also close to 1 if the estimated signal and the true signal are strongly correlated. Figure 7 shows these three diagnostics, averaged over the two-month experiment, for the four assimilations in GULFSTREAM (left columnn) and in OSMOSIS (right column). The PSD show very similar energy reconstruction at large scales for *EnKF no noise* and *EnKF karin noise* in both regions which is consistent with the previous RMSE results. Also, the relative error spectrum and the spectral coherence remain unaffected by the KaRIn noise. However, the PSD also show that the KaRIn noise degrades the small scale energy reconstruction, especially in the low energy region OSMOSIS. This result suggests that a pretreatment of the SWOT data to reduce the KaRIn error before assimilation might be needed. In GULFSTREAM, the spatially structured errors do not seem to have a significant impact on the reconstruction in terms of spectral diagnostics, especially for the PSD. This is probably due to the averaging over the two-month experiment in a very energetic region. Nonetheless, a slight improvement made by the detrended-DA scheme can be seen in terms of relative error spectrum and spectral coherence at mesoscale (100-200 km). In OSMOSIS, on the other hand, the full error strongly impacts the energy reconstruction at large scales. And, even if the spectral coherence is around 0.6 in the large scales the relative error spectrum shows that the PSD of the residue (i.e., estimate minus truth) is larger than the PSD of the truth, resulting in a negative relative error spectrum. The detrended-DA scheme restores a well estimated energy at large scales and significantly increases the relative error spectrum and spectral coherence at all scales.

In a nutshell, the spectral diagnostics confirm that the GULFSTREAM region is less impacted by the SWOT full noise than OSMOSIS which is explained by the large SSH variability in comparison to the noise variability and by the lower observation frequency in GULFSTREAM. Also, in terms of energy reconstruction, the PSD show that the detrended-DA entirely removes the impact of the correlated noises. The only difference left between the *EnKF detrended full noise* and the *EnKF no noise* is explained by the impact of the KaRIn noise on the small scales. Finally, in terms of relative error spectrum and spectral coherence, the full noise degrades the reconstruction at all scales but the reconstruction is well improved by the use of the detrending procedure from the large scales down to between 100km and 50km.

4 CONCLUSIONS

The goal of this study was to assess the embedding of the detrending procedure proposed by Metref et al. (2019) in an ensemble-based DA scheme in order to better assimilate the SWOT data with spatially structured errors. The assimilation problem proposed for that assessment was an OSSE for SSH field reconstruction using a one and a half layer QG model in two different regions: GULFSTREAM (spread from 33°N to 43°N and from 53°W to 65°) and OSMOSIS (spread from 45°N to 55°N and from 11°W to 19°W). By comparing EnKF assimilations of: (i) the noise free SWOT data, (ii) the KaRIn noise SWOT data, (iii) the fully noised SWOT data and (iv) the detrended fully noised SWOT data, the study has reached three major results.

The first major result is not directly related to the detrended-DA scheme assessed in this experiment but is a first answer to one of the major questions in the SWOT community (Rodriguez et al., 2017; Chelton et al., 2019; Morrow et al., 2019) about the impact of the KaRIn error on SWOT data assimilation. We have shown that, when assimilating SWOT data with an EnKF, the presence of KaRIn error does not have a significant effect on the SSH, the relative vorticity and the currents neither in terms of RMSE nor in terms of relative error spectrum and spectral coherence. However, the presence of KaRIn error slightly dampens the energy at small scales (under 200 km in GULFSTREAM and under 100 km in OSMOSIS). This result suggests that a pretreatment of the SWOT data to reduce the KaRIn error would help provide a better resolution of SWOT DA reconstructions in terms of energy.

The second major result is that, although in strongly energetic and less frequently observed regions such as GULFSTREAM the impact of the spatially structured errors may be marginal in average, the detrended-DA scheme can significantly reduce the RMSE at observation times. During an intensely observed time period, for instance, the SSH RMSE was reduced by up to 50%. The RMSE of relative vorticity and currents are also reduced by the detrended-DA scheme. This result shows that the detrended-DA scheme could be of crucial importance during the fast sampling phase where the SWOT satellite will have a 1 day revisit time and all regions of the globe will be instensely observed. The energy distribution throughout the spatial scales does not seem to be impacted by the spatially correlated errors. However, the detrended-DA scheme slightly improves the relative error spectrum and spectral coherence at mesoscale (100-200 km).

Finally, the third major result is the importance of assimilating a detrended SWOT data in less energetic regions such as OSMOSIS. The average SSH RMSE are more than halved when assimilating the detrended SWOT data rather than the raw data and the RMSE of relative vorticity and currents are significantly reduced as well. The signal energy at large and meso-scales is very well estimated and the relative error spectrum and spectral coherence are much improved by the detrended-DA scheme from the large scales down to small mesoscale (between 100km and 50km).

The study presented here was an OSSE that focused on the effects of the SWOT errors on the assimilation in the ocean surface using a QG model and the improvements brought by the detrended-DA scheme. Future works should expend this study by implementing a more complex assimilation system and assess the benefits of the detrended-DA scheme on the vertical component of the ocean. Also, as already stated in Metref et al. (2019), the detrending should be tested in larger regions with an adaptative computation in the along-track direction. Finally, as part of a larger challenge mobilizing the SWOT community, it will be crucial to investigate the behavior of the detrended-DA scheme in the presence of internal waves.

APPENDIX

The KaRIn instrumental error is simulated by the SWOT simulator (2016) as an uncorrelated zero-centered Gaussian noise of standard deviation dependent on the distance with the nadir. The standard deviation of the KaRIn noise is also dependent on the significant wave height (SWH) parameter which is a value between 0 and 8 meters. Figure 8 represents the standard deviation with respect to the distance with the nadir (in one half-swath only) and for different SWH parameters. The KaRIn error used in the present study was produced with the parameter SWH=2 m corresponding to the dark blue curve in Figure 8. As discussed in Section 3.1, this standard deviation was also used to prescribe the diagonal observation error covariance matrix $\mathbf{R}$ for the assimilation *EnKF karin noise* (directly) and for the assimilations *EnKF full noise* and *EnKF detrended full noise* (after inflation, see Section 3.1).

CONFLICT OF INTEREST STATEMENT

The authors declare that the research was conducted in the absence of any commercial or financial relationships that could be construed as a potential conflict of interest.

AUTHOR CONTRIBUTIONS

Sammy Metref, Emmanuel Cosme and Julien Le Sommer designed the study. Sammy Metref, Emmanuel Cosme, Julien Le Sommer and Jean-Michel Brankart designed the numerical experiments. Florian Le Guillou contributed to the implementation tools for the SWOT assimilation. Sammy Metref, Emmanuel Cosme, Julien Le Sommer and Florian Le Guillou contributed to the analysis of the results. Sammy Metref led the redaction of the manuscript and all authors contributed to the writing.

FUNDING

This research was funded by ANR (project number ANR-17-CE01-0009-01) and CNES through the OST/ST and the SWOT Science Team.

ACKNOWLEDGMENTS

The authors thank Maxime Ballarotta and Clément Ubelmann from CLS for the constructive discussions related to this study.

DATA AVAILABILITY STATEMENT

The datasets generated for this study are available on request to the corresponding author.

REFERENCES

Amores, A., Jordà, G., Arsouze, T., and Le Sommer, J. (2018). Up to what extent can we characterize ocean eddies using present-day gridded altimetric products? *Journal of Geophysical Research: Oceans* 123, 7220–7236. doi:10.1029/2018JC014140

Bishop, C. H., Etherton, B. J., and Majumdar, S. J. (2001). Adaptive sampling with the ensemble transform kalman filter. part i: Theoretical aspects. *Monthly Weather Review* 129, 420–436. doi:10.1175/1520-0493(2001)129⟨0420:ASWTET⟩2.0.CO;2

Brankart, J.-M., Ubelmann, C., Testut, C.-E., Cosme, E., Brasseur, P., and Verron, J. (2009). Efficient parameterization of the observation error covariance matrix for square root or ensemble kalman filters: Application to ocean altimetry. *Monthly Weather Review* 137, 1908–1927. doi:10.1175/2008MWR2693.1

Buckingham, C. E., Naveira Garabato, A. C., Thompson, A. F., Brannigan, L., Lazar, A., Marshall, D. P., et al. (2016). Seasonality of submesoscale flows in the ocean surface boundary layer. *Geophysical Research Letters* 43, 2118–2126. doi:10.1002/2016GL068009

Chelton, D. B., Ries, J. C., Haines, B. J., Fu, L.-L., and Callahan, P. S. (2001). Chapter 1 satellite altimetry. In *Satellite Altimetry and Earth Sciences*, eds. L.-L. Fu and A. Cazenave (Academic Press), vol. 69 of *International Geophysics*. 1 – ii. doi:https://doi.org/10.1016/S0074-6142(01)80146-7

Chelton, D. B., Schlax, M. G., Samelson, R. M., Farrar, J. T., Molemaker, M. J., McWilliams, J. C., et al. (2019). Prospects for future satellite estimation of small-scale variability of ocean surface velocity and vorticity. *Progress in Oceanography* 173, 256 – 350. doi:https://doi.org/10.1016/j.pocean.2018.10.012

Esteban-Fernandez, D. (2017). Swot project: Mission performance and error budget. revision a. *Jet Propulsion Laboratory Doc.* JPL D-79084

Fresnay, S., Ponte, A. L., Le Gentil, S., and Le Sommer, J. (2018). Reconstruction of the 3-d dynamics from surface variables in a high-resolution simulation of north atlantic. *Journal of Geophysical Research: Oceans* 123, 1612–1630. doi:10.1002/2017JC013400

Fu, L.-L. and Cazenave, A. (eds.) (2000). *Satellite altimetry and earth sciences: a handbook of techniques and applications*, vol. 69 (Elsevier)

Fu, L.-L. and Chelton, D. B. (2001). Chapter 2 large-scale ocean circulation. In *Satellite Altimetry and Earth Sciences*, eds. L.-L. Fu and A. Cazenave (Academic Press), vol. 69 of *International Geophysics*. 133 – viii. doi:https://doi.org/10.1016/S0074-6142(01)80147-9

Gaultier, L., Ubelmann, C., and Fu, L.-L. (2016). The challenge of using future swot data for oceanic field reconstruction. *Journal of Atmospheric and Oceanic Technology* 33, 119–126. doi:10.1175/JTECH-D-15-0160.1

Hunt, B. R., Kostelich, E. J., and Szunyogh, I. (2007). Efficient data assimilation for spatiotemporal chaos: A local ensemble transform kalman filter. *Physica D: Nonlinear Phenomena* 230, 112 – 126. doi:https://doi.org/10.1016/j.physd.2006.11.008. Data Assimilation

Liu, Z.-Q. and Rabier, F. (2002). The interaction between model resolution, observation resolution and observation density in data assimilation: A one-dimensional study. *Quarterly Journal of the Royal Meteorological Society* 128, 1367–1386. doi:10.1256/003590002320373337

Madec, G. (2015). Nemo ocean engine. *Note du Pôle de Modélisation; No 27; Institut Pierre-Simon Laplace (IPSL): Paris, France,* , 343–367

Metref, S., Cosme, E., Le Sommer, J., Poel, N., Brankart, J.-M., Verron, J., et al. (2019). Reduction of spatially structured errors in wide-swath altimetric satellite data using data assimilation. *Remote Sensing* 11. doi:10.3390/rs11111336

Miyoshi, T., Kalnay, E., and Li, H. (2013). Estimating and including observation-error correlations in data assimilation. *Inverse Problems in Science and Engineering* 21, 387–398. doi:10.1080/17415977.2012.712527

Morrow, R., Fu, L.-L., Ardhuin, F., Benkiran, M., Chapron, B., Cosme, E., et al. (2019). Global observations of fine-scale ocean surface topography with the surface water and ocean topography (swot) mission. *Frontiers in Marine Science* 6, 232. doi:10.3389/fmars.2019.00232

Morrow, R. and Le Traon, P.-Y. (2012). Recent advances in observing mesoscale ocean dynamics with satellite altimetry. *Advances in Space Research* 50, 1062 – 1076. doi:https://doi.org/10.1016/j.asr.2011.09.033. Oceanography, Cryosphere and Freshwater Flux to the Ocean

[Dataset] NATL60 (2018). meom-configurations/natl60-cjm165: Natl60 code used for cjm165 experiment (version v_1.0.0). zenodo: http://doi.org/10.5281/zenodo.1210116

Oke, P. R., Brassington, G. B., Griffin, D. A., and Schiller, A. (2008). The bluelink ocean data assimilation system (bodas). *Ocean Modelling* 21, 46 – 70. doi:https://doi.org/10.1016/j.ocemod.2007.11.002

Rodriguez, E., Fernandez, D. E., Peral, E., Chen, C. W., De Bleser, J.-W., and Williams, B. (2017). Wide-swath altimetry: a review. In *Satellite Altimetry Over Oceans and Land Surfaces* (CRC Press). 71–112

Ruggiero, G. A., Cosme, E., Brankart, J.-M., Le Sommer, J., and Ubelmann, C. (2016). An efficient way to account for observation error correlations in the assimilation of data from the future swot high-resolution altimeter mission. *Journal of Atmospheric and Oceanic Technology* 33, 2755–2768. doi:10.1175/JTECH-D-16-0048.1

Stammer, D. and Cazenave, A. (eds.) (2018). *Satellite Altimetry Over Oceans and Land Surfaces.* (Boca Raton: CRC Press). doi:https://doi.org/10.1201/9781315151779

Stewart, L. M., Dance, S. L., and Nichols, N. K. (2008). Correlated observation errors in data assimilation. *International Journal for Numerical Methods in Fluids* 56, 1521–1527. doi:10.1002/fld.1636

Stewart, L. M., Dance, S. L., and Nichols, N. K. (2013). Data assimilation with correlated observation errors: experiments with a 1-d shallow water model. *Tellus A: Dynamic Meteorology and Oceanography* 65, 19546. doi:10.3402/tellusa.v65i0.19546

[Dataset] SWOT simulator (2016). Ocean swot simulator. jet propulsion laboratory. github: https://github.com/swotsimulator

Ubelmann, C., Klein, P., and Fu, L.-L. (2015). Dynamic interpolation of sea surface height and potential applications for future high-resolution altimetry mapping. *Journal of Atmospheric and Oceanic Technology* 32, 177–184. doi:10.1175/JTECH-D-14-00152.1

Waller, J. A., Dance, S. L., Lawless, A. S., and Nichols, N. K. (2014). Estimating correlated observation error statistics using an ensemble transform kalman filter. *Tellus A: Dynamic Meteorology and Oceanography* 66, 23294. doi:10.3402/tellusa.v66.23294

Yaremchuk, M., D'Addezio, J. M., Panteleev, G., and Jacobs, G. (2018). On the approximation of the inverse error covariances of high-resolution satellite altimetry data. *Quarterly Journal of the Royal Meteorological Society* 144, 1995–2000. doi:10.1002/qj.3336

	GULFSTREAM				OSMOSIS			
	SSH	ζ	u	v	SSH	ζ	u	v
EnKF no noise.	0.093	0.281	0.201	0.203	0.019	0.127	0.057	0.062
EnKF karin noise	0.094	0.283	0.204	0.207	0.020	0.127	0.058	0.062
EnKF full noise	0.121	0.308	0.224	0.255	0.064	0.182	0.095	0.162
EnKF detrended full noise	0.109	0.298	0.216	0.229	0.029	0.134	0.065	0.079

Table 1. RMSE averaged over the 2 month experiment for the four assimilations in GULFSTREAM and OSMOSIS for SSH (in meters), ζ (adimensional), u (in m/s) and v (in m/s).

FIGURE CAPTIONS

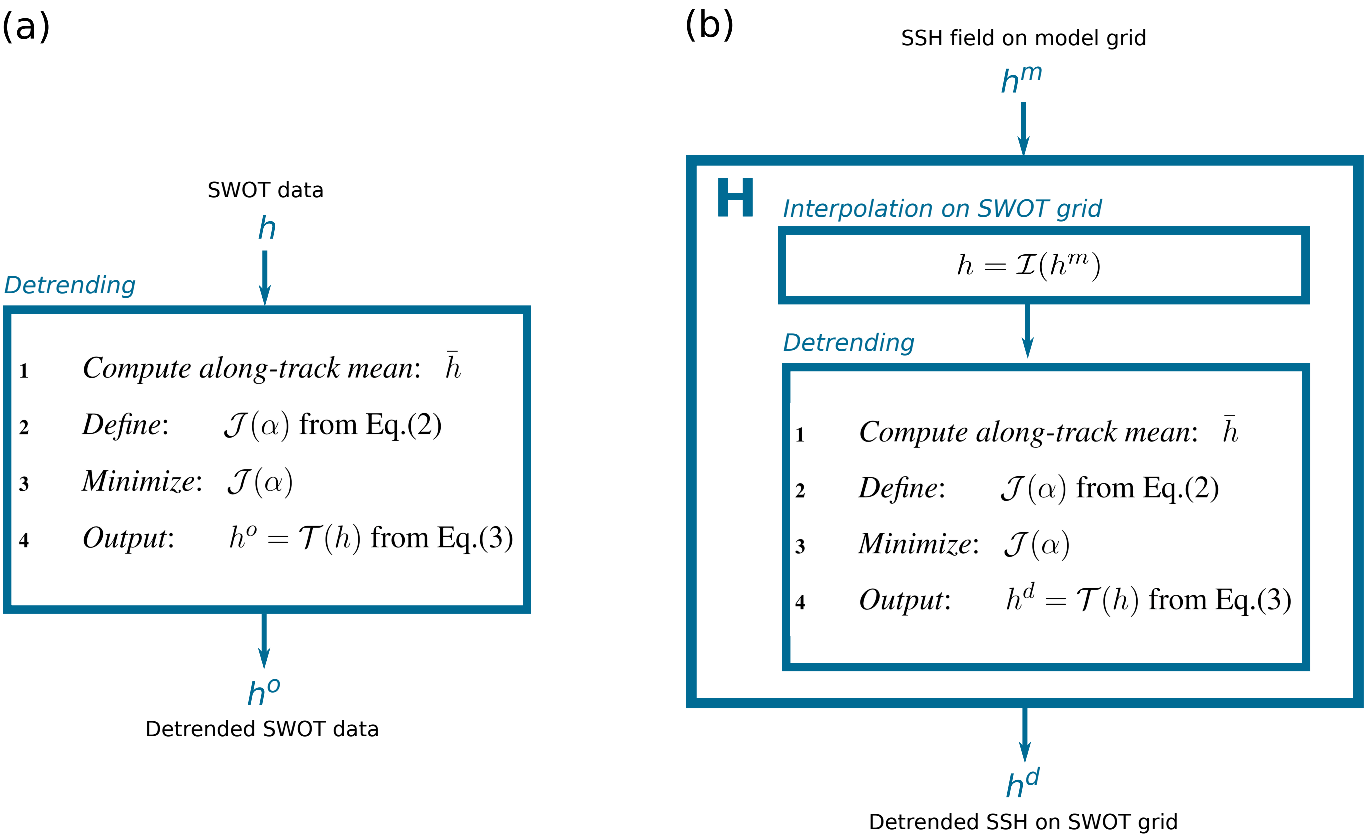

Figure 1. Algorithms for (a) the SWOT data detrending and (b) the embedding of the detrending in the observation operator H (see Equation 4).

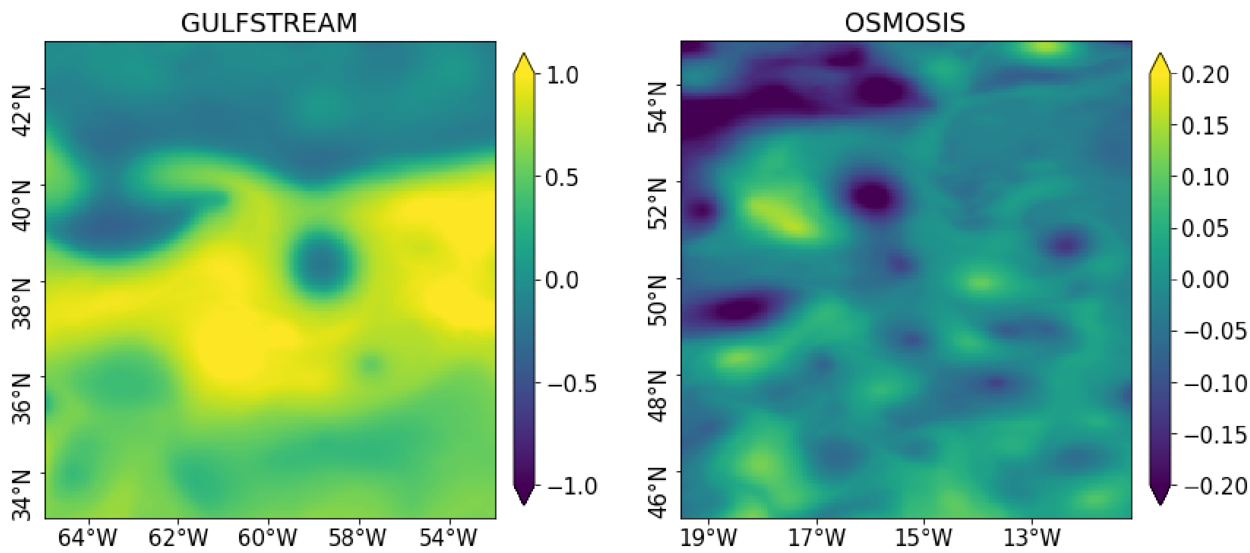

Figure 2. SSH fields (in meters), in the two regions of interest: GULFSTREAM (left panel) and OSMOSIS (right panel), on November 4, 2012.

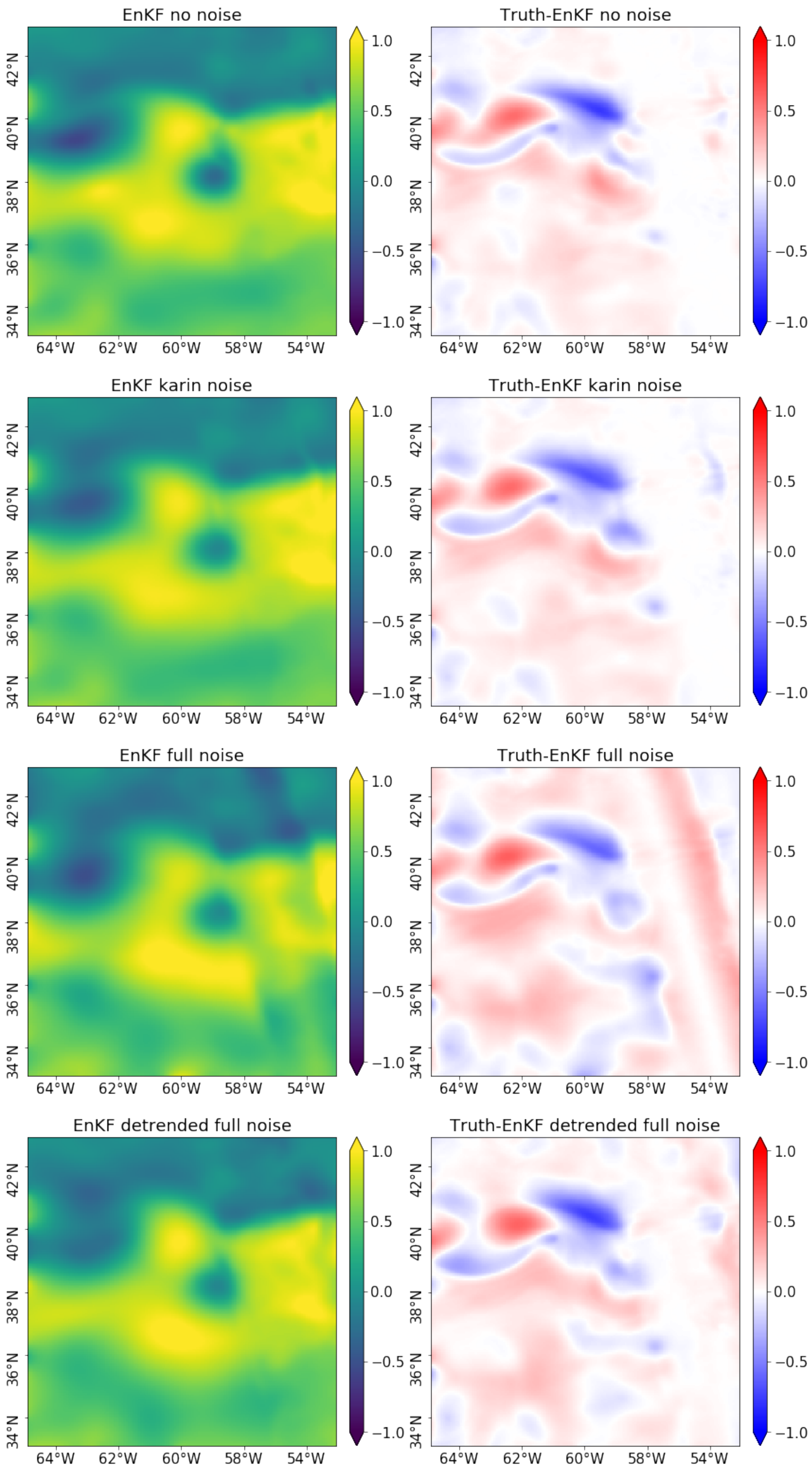

Figure 3. SSH field reconstructions (left column), in GULFSTREAM, performed by the four assimilations and their differences (right column) to the true state on November 4, 2012 displayed in Figure 2.

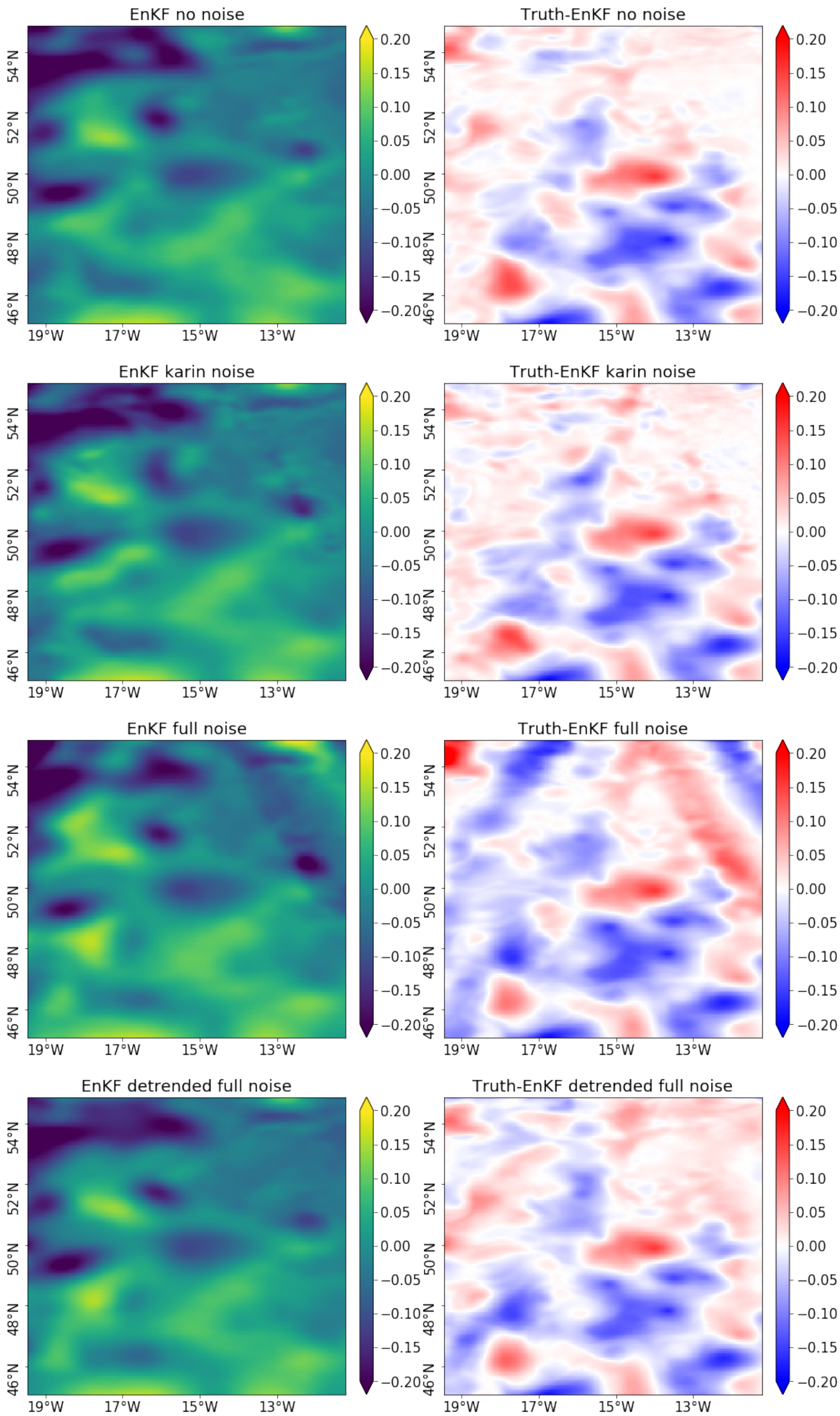

Figure 4. Same as Figure 3 but in OSMOSIS.

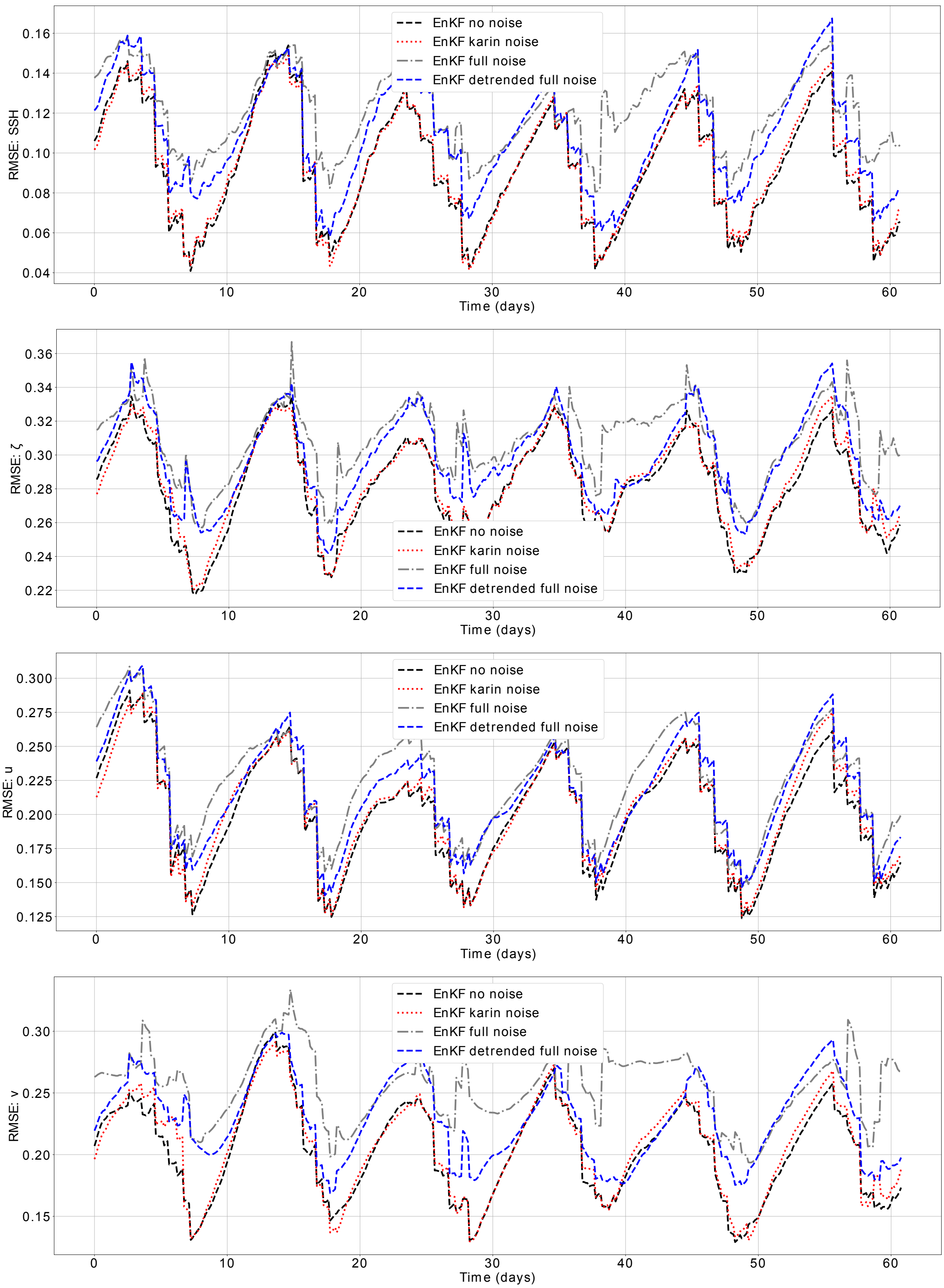

Figure 5. RMSE time series for the four assimilations during the 2 month experiment in GULFSTREAM for SSH (first line), ζ (second line), u (third line) and v (fourth line).

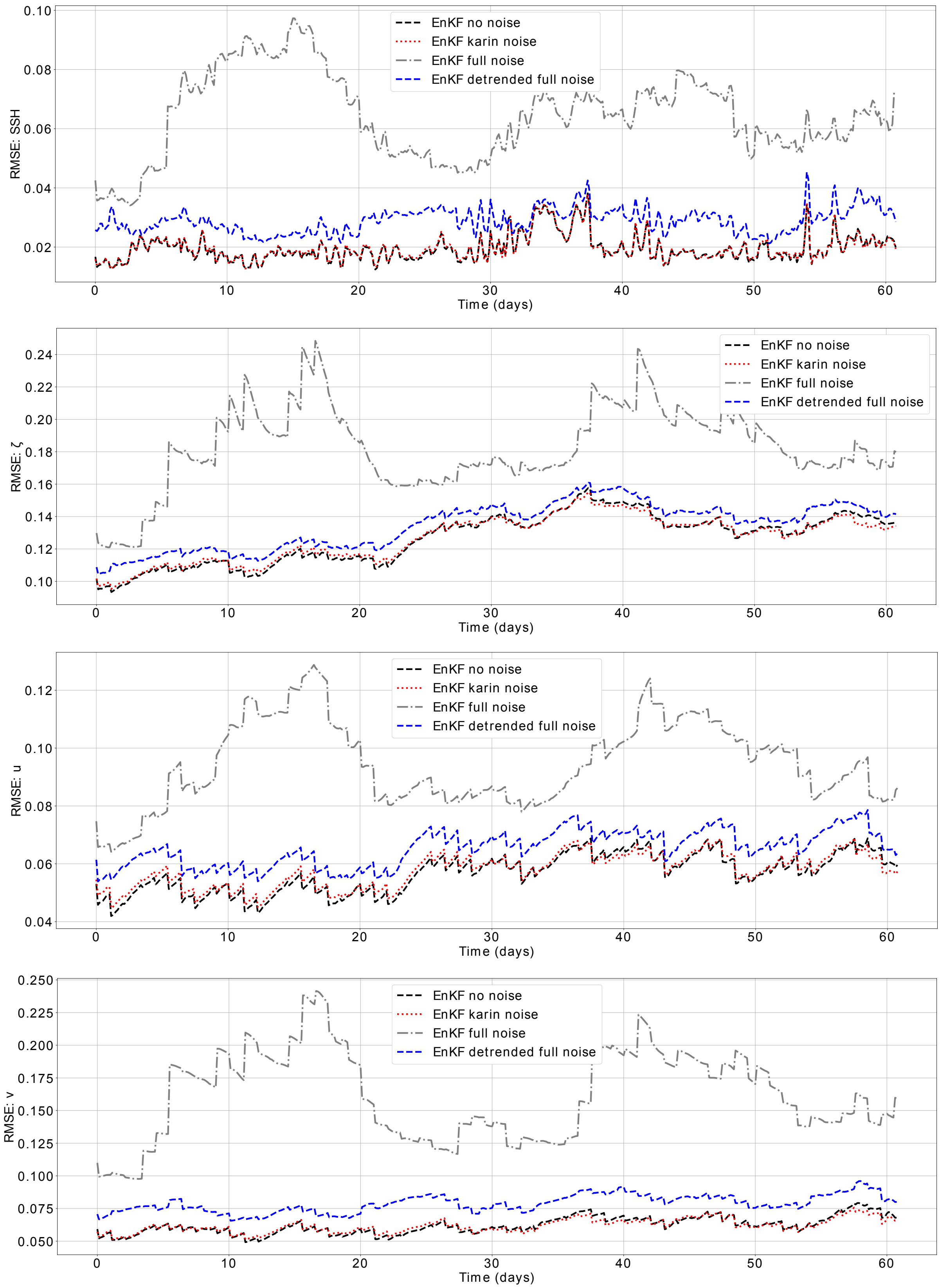

Figure 6. Same as Figure 5 but in OSMOSIS.

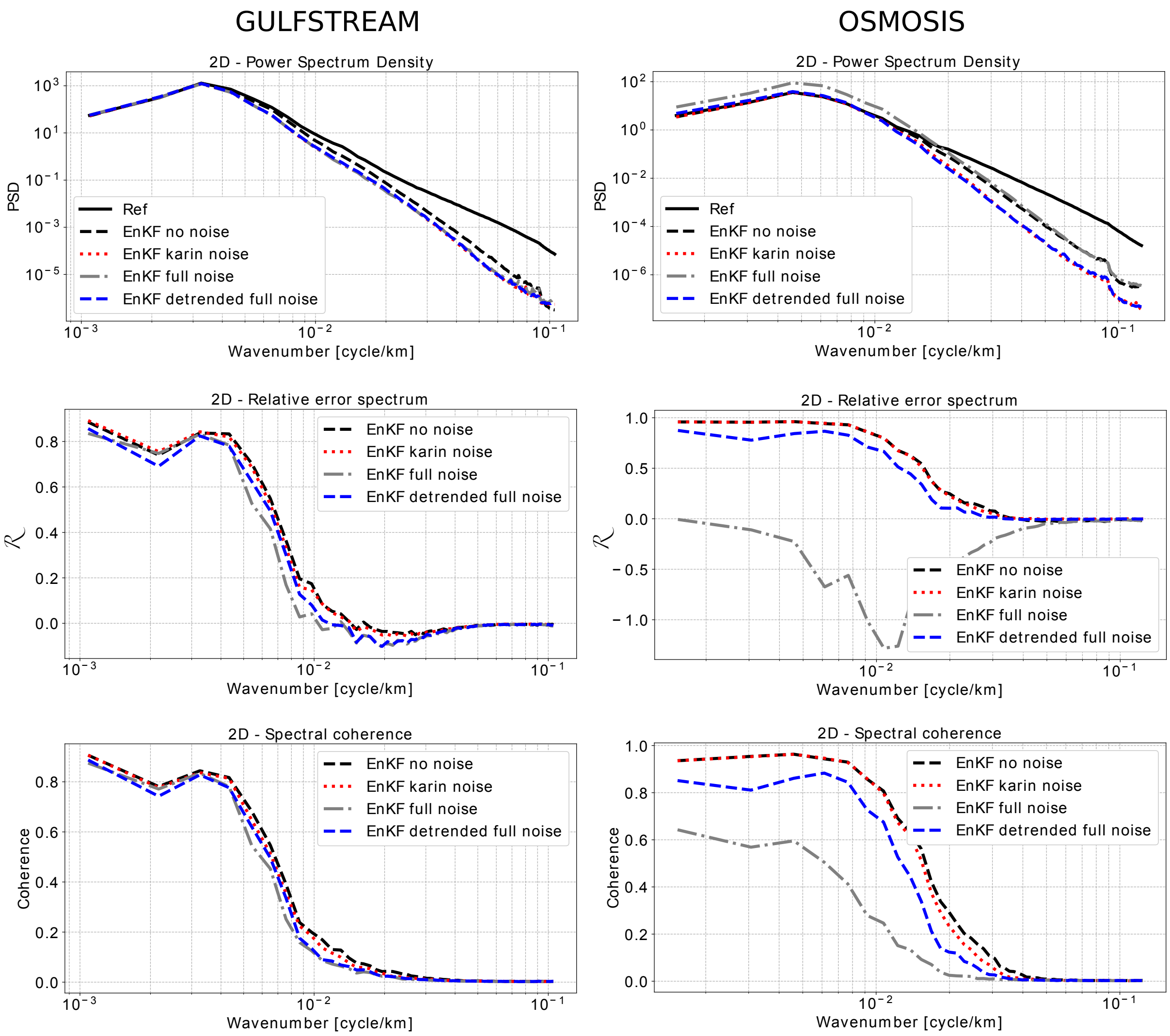

Figure 7. Power spectral density (first line), relative error spectrum (second line) and spectral coherence (third line) on SSH, for the four assimilations, averaged during the 2 month experiment in GULFSTREAM (left column) and OSMOSIS (right column).

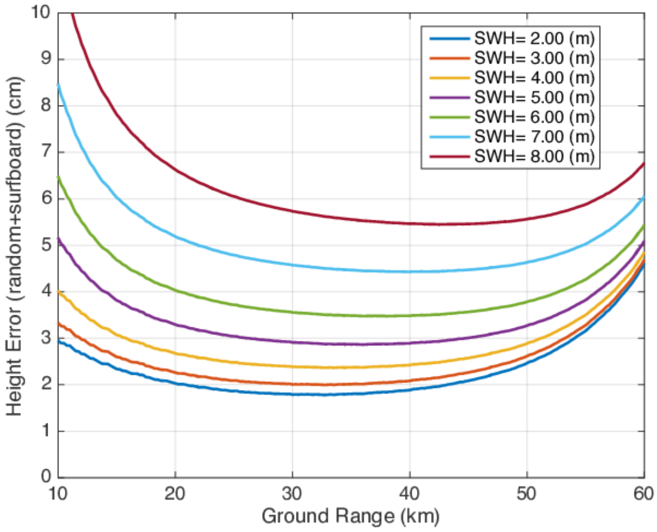

Figure 8. [Figure extracted from the SWOT simulator (2016) manual] The example curves of the standard deviation (cm) of the KaRIN noise as a function of cross-track distance (km).